

Annual Cycle and Depth Penetration of Wind-Generated Near-Inertial Internal Waves at Ocean Station Papa in the Northeast Pacific

MATTHEW H. ALFORD

Applied Physics Laboratory, and School of Oceanography, University of Washington, Seattle, Washington

MEGHAN F. CRONIN

National Oceanic and Atmospheric Administration/Pacific Marine Environmental Laboratory, Seattle, Washington

JODY M. KLYMAK

School of Earth and Ocean Sciences, University of Victoria, Victoria, British Columbia, Canada

(Manuscript received 10 May 2011, in final form 1 October 2011)

ABSTRACT

The downward propagation of near-inertial internal waves following winter storms is examined in the context of a 2-yr record of velocity in the upper 800 m at Ocean Station Papa. The long time series allow accurate estimation of wave frequency, whereas the continuous data in depth allow separation into upward- and downward-propagating components. Near-inertial kinetic energy (KE_{in}) dominates the record. At all measured depths, energy in downgoing motions exceeds that of upward-propagating motions by factors of 3–7, whereas KE_{in} is elevated by a factor of 3–5 in winter relative to summer. The two successive winters are qualitatively similar but show important differences in timing and depth penetration. Energy is seen radiating downward in a finite number of wave groups, which are tagged and catalogued to determine the vertical group velocity c_{gz} , which has a mean of about $1.5 \times 10^{-4} \text{ m s}^{-1}$ (13 m day^{-1}). Case studies of three of these are presented in detail.

Downward energy flux is estimated as $c_{gz} \times KE_{in}$ (i) by summing over the set of events, (ii) from time series near the bottom of the record, and (iii) from the wavenumber–frequency spectrum and the dispersion relationship. These estimates are compared to the work done on near-inertial motions in the mixed layer by the wind, which is directly estimated from mixed layer near-inertial currents and winds measured from a surface buoy 10 km away. All three methods yield similar values, indicating that 12%–33% of the energy input into the mixed layer transits 800 m toward the deep sea. This simple picture neglects lateral energy flux carried by the first few vertical modes, which was not measured. The substantial deep penetration implies that near-inertial motions may play a role in mixing the deep ocean, but the strong observed variability calls for a need to better understand the role of lateral mesoscale structures in modulating the vertical propagation.

1. Introduction

Near-inertial waves (NIW), generated primarily when winter storms blow on the ocean surface mixed layer, are one of the two most energetic portions of the internal wave band (internal tides are the other). Several calculations indicate that the work done on near-inertial motions in the mixed layer by the wind is 0.3–1.4 TW (Alford 2001b, 2003b; Watanabe and Hibiya 2002; Jiang et al. 2005), a substantial portion of the 2 TW needed to

maintain the abyssal stratification (Munk and Wunsch 1998; Wunsch and Ferrari 2004) and comparable to conversion of energy from the barotropic tide to internal tides (Egbert and Ray 2000, 2001), demonstrating their potential importance in mixing the deep ocean. Because shear rather than velocity and energy is key for leading to wave breaking and mixing, mixing is envisioned to occur either through a spectral cascade involving wave–wave interactions (e.g., Gregg et al. 2003) or through direct breaking of the smaller-scale waves (Alford and Gregg 2001; Alford 2010).

Of critical importance to this argument is the downward energy flux, because, if the waves dissipate in the upper ocean, little energy is left for mixing the abyss

Corresponding author address: Matthew H. Alford, Applied Physics Laboratory, 1013 NE 40th St., Seattle, WA 98105.
E-mail: malford@apl.washington.edu

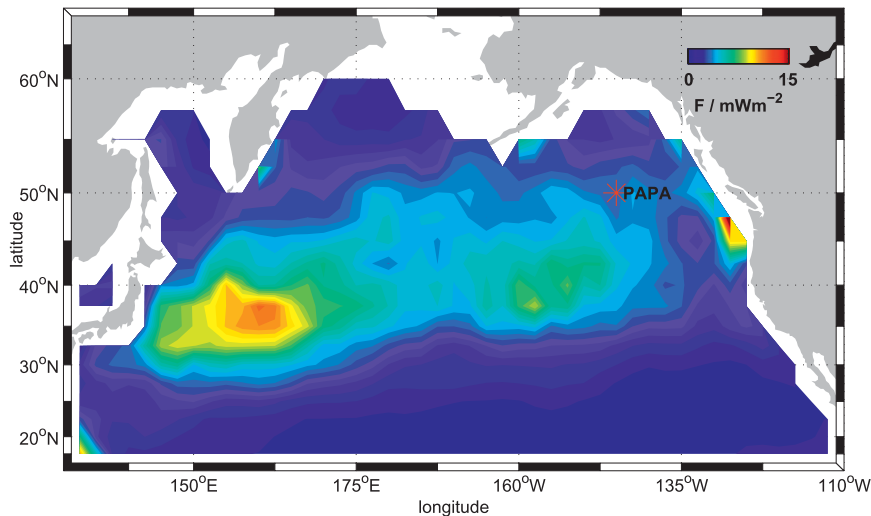


FIG. 1. Map of the north Pacific showing the location of the Papa moorings. Colors give annual-mean energy flux computed from NCEP winds and the Pollard–Millard slab model (Alford 2003b).

(though bottom-generated NIW could still play a role). Just this conclusion was reached by a numerical study by Furuichi et al. (2008), which indicated that 85% of the near-inertial energy deposited into the mixed layer by the wind was dissipated in the upper 150 m. Because this is seemingly at odds with the observed seasonal cycle of near-inertial energy at all depths down to a few hundred meters above bottom (Mihaly et al. 1998; Alford and Whitmont 2007; van Haren 2007; Silverthorne and Toole 2009) and the significant equatorward energy flux in low-mode near-inertial waves (Alford 2003a), quantitative measures of the vertical and lateral energy flux are needed to reconcile these two views.

Partly because of these issues, the near-inertial wave wake of fast-moving storms has been studied in some detail. The process is envisioned in two stages: first a brief initial phase whereby the momentum is rapidly deposited in the mixed layer, followed by the adjustment of the interior. The first stage is fairly well understood, beginning with the pioneering work of D’Asaro (1985), continuing with the wind work calculations mentioned above, and culminating with the observations and analysis of Plueddemann and Farrar (2006). The second stage was first treated theoretically by Gill (1984), who projected the slab mixed layer velocity onto vertical dynamical modes over a flat bottom. Because the storm sets the lateral scale, the modes all have different frequencies by the dispersion relation,

$$\omega_n^2 - f^2 = c_n^2 K^2, \quad (1)$$

where c_n and K are the phase speed and horizontal wavenumber of mode n . Because purely inertial motions

do not propagate vertically or horizontally, the frequency difference from the inertial frequency f plays a major role in near-inertial propagation.

As the modes rotate relative to one another, energy migrates downward from the mixed layer (the propagation may equivalently be thought of in terms of vertically propagating rays; Kroll 1975; Zervakis and Levine 1995; Garrett 2001). Gill’s analysis initially presented a puzzle because the large scale of synoptic storms resulted in frequencies very close to inertial [from (1)] and therefore very slow propagation. D’Asaro (1989) demonstrated that the β effect rapidly introduces the needed smaller scales as motions at different latitudes rotate relative to one another, with mesoscale mixed layer motions also playing a role (Weller 1982; Young and Ben Jelloul 1997; Moehlis and Llewellyn-Smith 2001). The general correctness of these physics was demonstrated for the low modes by detailed observations and analysis of D’Asaro et al. (1995) and D’Asaro (1995a,b). However, the higher modes, which contain most of the shear, were not well described by the theory.

With these issues in mind, we here examine data from a recent 2-yr deployment of two acoustic Doppler current profilers (ADCPs) on a subsurface mooring at Ocean Station Papa (Figs. 1, 2). The instruments measure velocity each $\frac{1}{2}$ hour in 4-m bins in the upper 130–200 m and 16-m bins below that, allowing estimation of continuous profiles of kinetic energy, its separate upward- and downward-propagating components, and clear identification of the structure of wave groups. These are seen propagating downward at all depths to the bottom of our array at 800 m. The long time series allow isolation of near-inertial

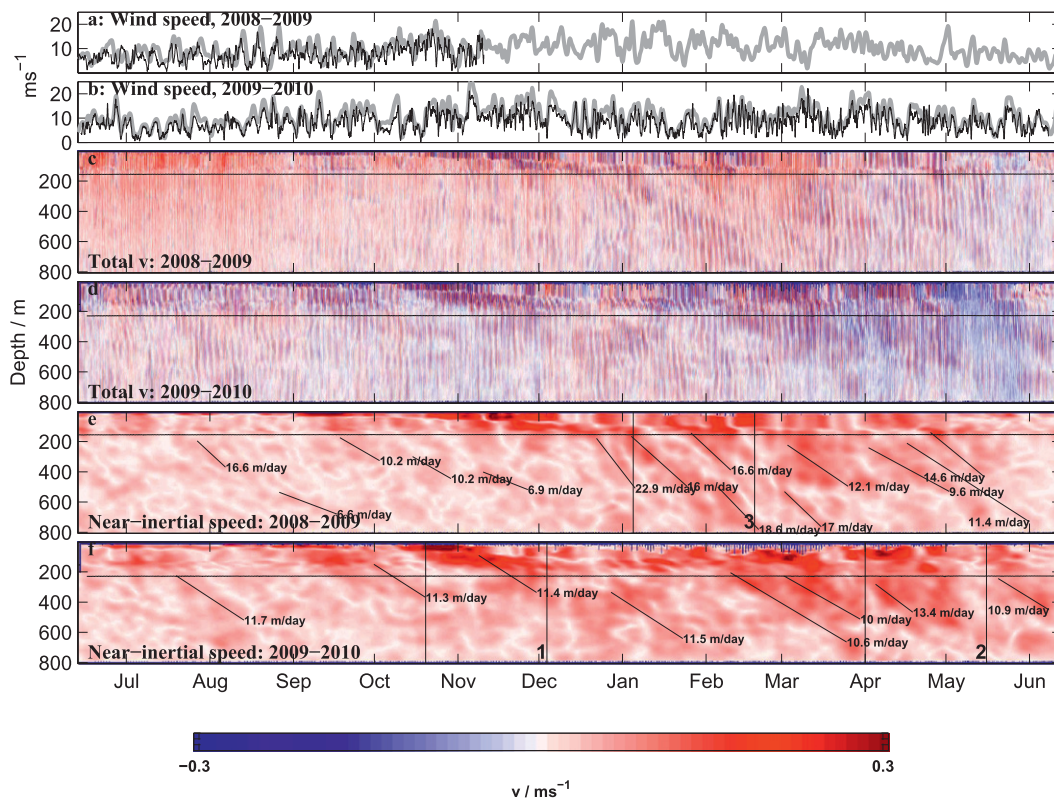


FIG. 2. Wind speed, measured meridional velocity, and near-inertial speed for the entire 2-yr record for (a),(c),(e) the first year and (b),(d),(f) second year. (a),(b) Wind speed measured at the surface buoy (black) and from NCEP reanalysis (gray); (c),(d) meridional velocity; and (e),(f) near-inertial speed obtained by bandpassing (see text). The measured depth of the upper ADCP is indicated in each panel. In (e),(f), downward migration of each identified event (see text) is indicated with downward-sloping lines. The implied downward group velocity of each is indicated. Closeup periods plotted in Figs. 13–15 are shown.

signals and accurate estimation of wave frequency, which we use to determine group velocity. Though these estimates of vertical group velocity are uncertain, they are used together with the energy profiles to estimate the vertical flux of energy. This is finally compared to the observed wind work computed from our observed near-inertial mixed layer velocities and wind and mixed layer depth (MLD) measured at the Papa surface mooring 10 km away. We find that a substantial fraction of the energy input into the mixed layer passes 800 m, suggesting that this energy reaches the deep sea. However, important differences exist in the timing and character of the energy penetration during the two winters, highlighting the need to understand the lateral scales of the forcing and mixed layer motions.

2. Data and techniques

a. Moorings

Data are from a surface mooring and a subsurface mooring maintained at ocean station Papa (Fig. 1) by the

National Oceanic and Atmospheric Administration/Pacific Marine Environmental Laboratory (NOAA/PMEL). The subsurface mooring was deployed on 13 June 2008 and operated continuously until 14 June 2010, except for a 2-day gap in June 2009 during its turnaround. The surface mooring, 10 km away, measured wind and other meteorological quantities every 10 min until 11 November 2008, when it broke free and drifted away. Subsurface measurements were lost. In June 2009 it was replaced and delivered wind (Figs. 2a,b) and subsurface temperature and salinity from 0 to 120 m until June 2010 (Fig. 4c).

b. Velocity measurements

Velocity was measured on the subsurface mooring via two ADCPs (Figs. 2c,d). A 75-KHz unit looking upward from 800 m measured velocity in 16-m bins. A shallower unit, which in year 1 was an uplooking 300-KHz system at 154 m and in year 2 was an uplooking 150-KHz system at 227 m, sampled the upper ocean in 4-m bins. Each instrument formed ensembles every 30 min, which each consisted of 10 pings in rapid succession.

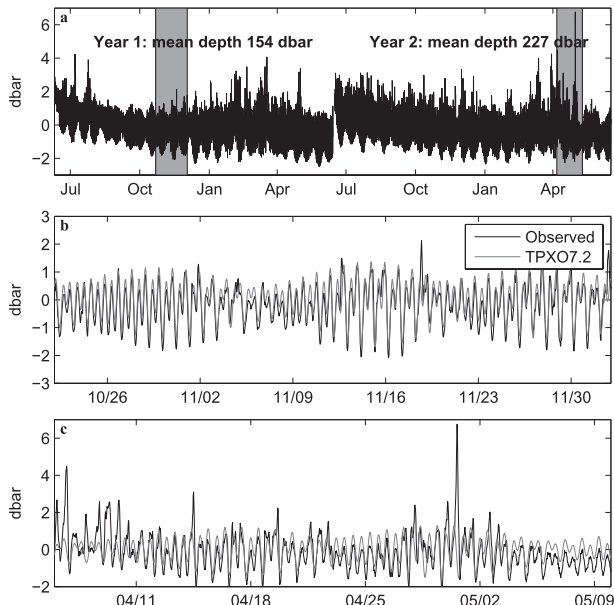


FIG. 3. Pressure measured at the top ADCP (a) for the whole record and (b),(c) for the two sample periods indicated in (a) in gray. The time-mean for each year, indicated in (a), is subtracted before plotting. In (b),(c), the tidal elevation prediction from TPXO7.2 is also plotted in gray.

As indicated by the pressure measured at the shallow instrument (black), mooring layover was minimal, because of a taut design and generally moderate currents below the mooring's top. To demonstrate this in more detail, measured pressure at the upper ADCP is plotted in Fig. 3 after first subtracting out the mean pressure in each year. Observed pressure differences for the whole record (Fig. 3a) demonstrate that the ADCP is always within 6.5 m of its target depth. Observed deviations arise from (i) the slow creep of about 2 m during the first few months of the Vectran mooring line, (ii) variations in sea surface elevation due to the tides, and (iii) layovers of the mooring due to strong currents. From the two closeup plots (Figs. 3b,c), it is clear that observed pressure closely follows tidal elevation predictions from the Oregon State Ocean Topography Experiment (TOPEX)/Poseidon 7.2 (TPXO7.2) tidal inverse model (Egbert and Erofeeva 2002), with typical peak–peak signals of 3 dbar. During the worst layovers of the entire record (Fig. 3c), strong currents cause the mooring top to dive 6.5 m below its usual depth. This is far too little to affect our measurements.

Returning to Fig. 2, slight discontinuities in velocity are visible at the seam between the two instruments, about 20 m above the depth of the shallow instrument. These are partly due to the difference in bin size and noise floor of the two instruments and partly because the beams of the lower instrument are separated by about 400 m at this depth. Hence, the two instruments are

sampling slightly different water. Though these scars are visible in the raw velocity, they do not affect our results.

The upper 10% of the profiling range of the upper ADCP (15 and 22 m in years 1 and 2) is discarded because of contamination by the surface reflection of the sidelobe transmission. During April–December of the second year, low scattering levels led to poor range, resulting in occasional surface gaps up to 100 m.

c. Bandpassing

Inertial velocities $Z_{in} \equiv u_{in} + iv_{in}$ are isolated by means of a fourth-order Butterworth filter applied in the time domain. The filter is applied twice, once forward and once backward, to minimize distortion of phase. Upper and lower limits are $\{0.9, 1.15\}f$. The near-inertial parts of the signals for the full 2-yr records are seen in Figs. 2e,f.

d. Mixed layer depth

Temperature and salinity measured at 11 depths on the surface mooring were used to estimate the mixed layer depth during the second year. Potential density σ_θ is first computed from temperature and salinity and interpolated onto a uniform depth grid (Fig. 4b). MLD (black line) is then computed, following the usual convention (e.g., Levitus and Boyer 1994), because the first depth at which measured potential density exceeds the surface value by 0.125 kg m^{-3} . Because diel convection is not our focus, MLD is smoothed over 10 days.

A second estimate of MLD comes from the depth to which momentum is mixed. Returning to Figs. 2c,d, the mixed layer is evident as a region of uniform velocity 20–30 m thick in summer, deepening to about 120 m each fall and shoaling in late spring each year back to 20 m. The deepest extent of the region is determined by calculating the minimum depth at which shear magnitude exceeds 0.45 s^{-1} . The shear-based estimate of MLD (Fig. 4b, gray line) agrees well with the density-based estimate but is often about 10 m deeper, following other reports of momentum penetration beyond the scalar mixed layer (Johnston and Rudnick 2009).

e. Stratification

Deeper than these measurements, temperature and salinity were only measured at 500 and 700 m. Buoyancy frequency, $N(z) = [-(g/\bar{\rho})(\partial\sigma_\theta/\partial z)]^{1/2}$, where $\bar{\rho}$ is the mean potential density, is therefore from CTD casts taken on the deployment and recovery cruises (Fig. 5a). Because these were in summer, another CTD profile taken a few hundred kilometers to the east in February 2010 is plotted for comparison. Observed profiles are in good agreement with climatological values from Levitus and Boyer (1994), decreasing only by about a factor of 1.5 from 200 to 800 m (inset).

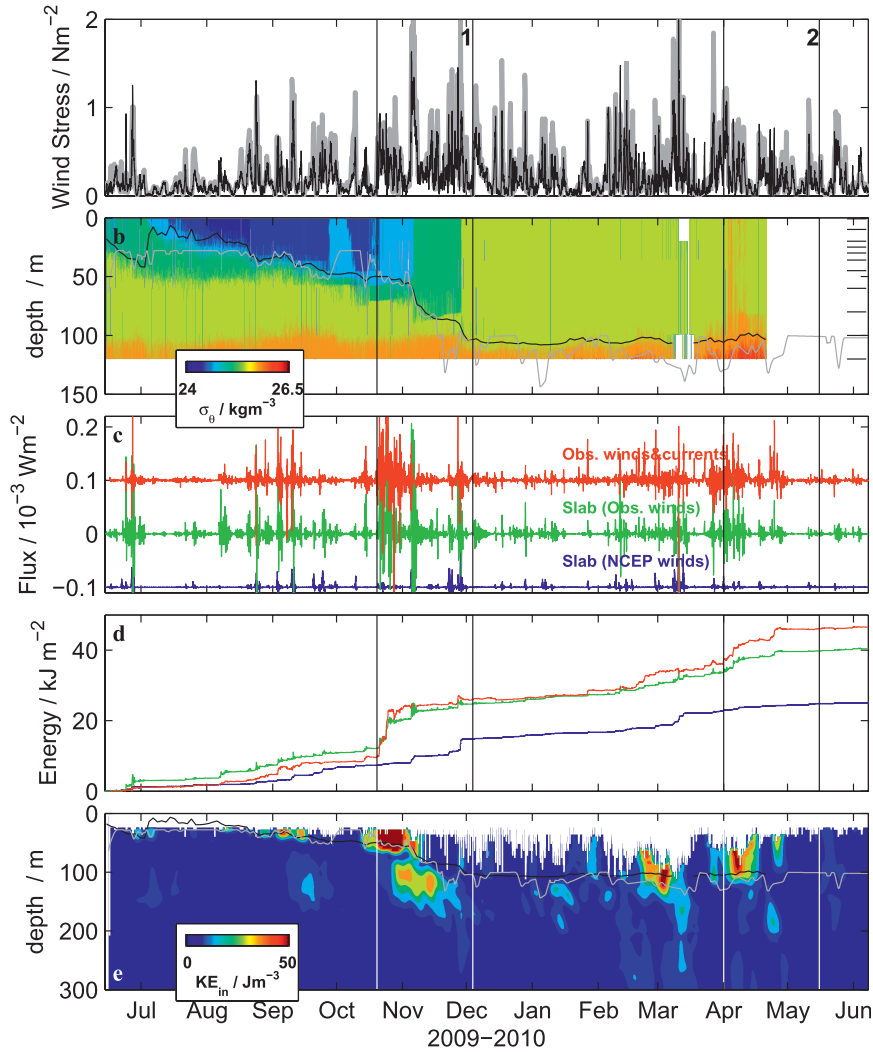


FIG. 4. (a) Wind stress computed using the Large and Pond (1981) wind stress parameterization from NCEP reanalysis winds (gray) and measured at the surface buoy (black). (b) Potential density measured from Sea-Bird Electronics MicroCATs on the surface buoy (depths indicated at right). Time series of MLD determined from density (black) and shear (gray) are overplotted; see text. (c) Wind work computed from the slab model driven with NCEP and measured winds (blue and green) and from measured winds and inertial currents (red). Successive traces are offset by 0.1. (d) The time integral of (c) showing the cumulative energy input to the mixed layer from each flux estimate. (e) Inertial KE in the upper 300 m. The two MLD estimates from (b) are replotted. Periods examined in detail are indicated with vertical bars.

Internal waves adjust their amplitude and wavenumber as they undergo refraction in variable stratification. To minimize these effects, the climatological profile is used to “Wentzel–Kramers–Brillouin (WKB) scale” and “WKB stretch” observed velocities, following Leaman and Sanford (1975). Velocity is multiplied by a factor of $[N(z)/\langle N \rangle]^{1/2}$ (Fig. 6b, gray), where $\langle N \rangle = 3.6 \times 10^{-3} \text{ rad s}^{-1}$ is the mean climatological stratification computed between 120 and 800 m (Fig. 6a). The resulting factor in energy is $[N(z)/\langle N \rangle]$.

To account for wavenumber changes, WKB-stretched depth is computed as

$$z' = \int_{120}^z \frac{N}{\langle N \rangle} dz. \quad (2)$$

Integration is begun at the deepest observed mixed layer depth of 120 m to avoid complications with time-variable mixed layer depth. Above that, stretched and unstretched depths are equal (Fig. 6c). Depth–time maps are plotted

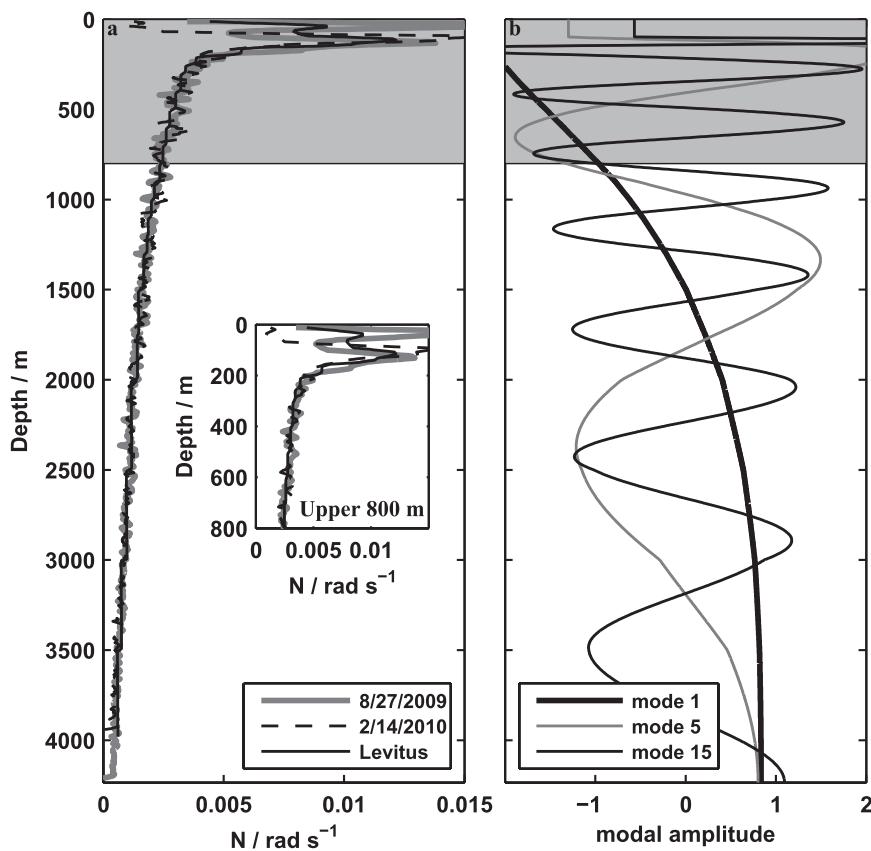


FIG. 5. (a) Buoyancy frequency computed over 8-m intervals from temperature and salinity measured from two line P cruises (gray and dashed lines) and from Levitus (thin black line). The upper 800 m spanned by our measurements is shaded in gray and plotted in the inset. (b) Vertical structure of dynamical modes 1, 5, and 15. Gray is the depth range of our observations.

versus unstretched depth, but quantitative calculations such as the spectrum and vertical group velocity are computed in stretched coordinates.

f. Wind work

The work done by the wind on mixed layer motions in the mixed layer can most directly be computed as the dot product of the measured near-inertial winds and mixed layer currents,

$$\Pi_{\text{obs}} = \tau_{\text{in}} \cdot \mathbf{u}_{\text{in}}. \quad (3)$$

This expression is obtained by bandpass filtering the equations of motion (Silverthorne and Toole 2009).

Because simultaneous observations of mixed layer velocity and wind are relatively rare, several past studies have employed a slab model developed by Pollard and Millard (1970) to obtain more indirect estimates of the near-inertial mixed layer velocity \mathbf{u}_{slab} from time series of wind alone.

Here, \mathbf{u}_{slab} is proportional to the inverse of the mixed layer depth H , which is normally taken from a climatology (D'Asaro 1985; Alford 2001b, 2003b; Watanabe and Hibiya 2002; Jiang et al. 2005). The wind work is then obtained either via (3) or by means of an energy equation derived by D'Asaro (1985). For a slab model with purely inertial forcing, the two expressions are equal (Plueddemann and Farrar 2006); in practice, they differ by <10%–15% (Alford 2003b), indicating the dominance of resonant forcing by inertially rotating winds at midlatitudes.

In this study, we use (3) to compute wind work three ways, in decreasing order of accuracy. For the second year when we have measurements of both mixed layer velocity and wind, we avoid the complications and assumptions of the slab model and compute the wind work directly from (3). For comparison, we also evaluate the slab model using observed winds using the spectral method given in Alford (2003b) and compute work by substituting the slab velocity for the measured near-inertial velocity in (3). A third estimate results from using National

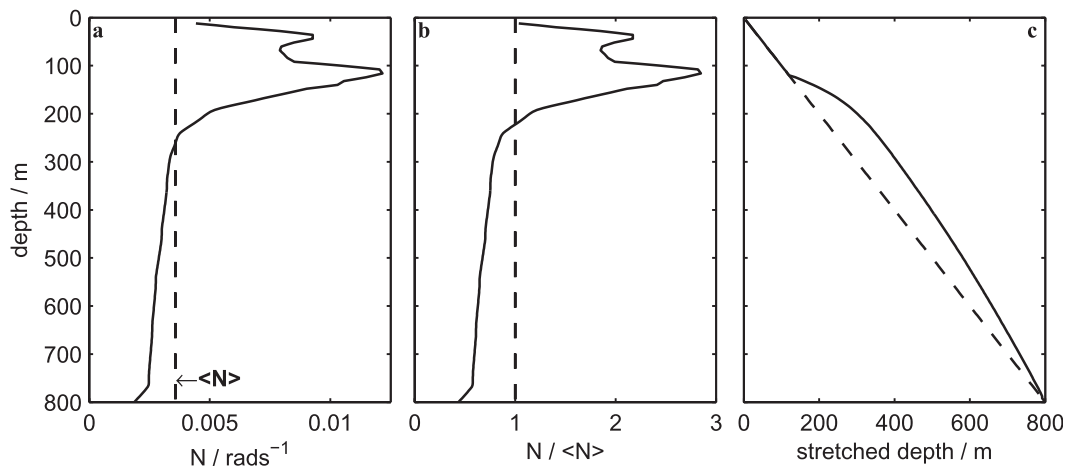


FIG. 6. WKB scaling and stretching calculations. (a) Climatological stratification in the upper 800 m. Dashed line indicates the mean from 120 to 800 m. (b) The WKB scaling factor $N(z)/\langle N \rangle$. (c) WKB-stretched depth. The dashed line shows the unstretched depth for reference.

Centers for Environmental Prediction (NCEP) reanalysis winds instead of observed winds (because buoy winds are unavailable for year 1). Observed momentum-based mixed layer depth is used for all slab-model calculations, smoothed over 10 days. Rayleigh damping is applied in the slab model with a value of $r = 1/(20 \text{ days})$.

A comparison of the three estimates is given in Figs. 4c,d. In Fig. 4c, each estimate of wind work is shown, offset by 0.1 W m^{-2} , with the time integral, showing cumulative energy input, in Fig. 4d. As demonstrated by D’Asaro (1985), net work is done on the ocean by the wind, with peaks in late winter/spring. Work is quite intermittent, with a large portion of the energy input in only a few events. Most wind work events occur at the same time in the two measured quantities (e.g., events in late November 2008 and April 2009). The NCEP quantity replicates some but not all of them (showing, for example, neither of these two events), giving an annual mean only half of the estimates using the observed winds.

Recent direct comparisons by Plueddemann and Farrar (2006) between observed and slab-model wind work suggested that the slab model, in spite of accurately reproducing amplitude and phase of the velocity response, often overestimated work because of its neglect of dissipative processes at the base of the mixed layer. The Price et al. (1986) model, which better incorporates these processes, replicated the observed wind work more closely. In our data, observed wind work Π_{obs} and slab work Π_{slab} computed from buoy winds agree fairly well. Their annual means are within 10% of each other, contrasting somewhat with Plueddemann and Farrar (2006). However, the two studies are not directly comparable, because Plueddemann and Farrar (2006) used slightly different expressions for both the observed and

slab-model work. Because the slab calculations are not our focus and do not affect our results, we leave more detailed comparisons to future studies.

g. Linear response

The structure of near-inertial waves propagating into the interior is a complicated function of the lateral geometry of the forcing (Gill 1984) and mesoscale mixed layer currents (Weller 1982; Young and Ben Jelloul 1997; Moehlis and Llewellyn-Smith 2001). However, the energy is partitioned into vertical modes in a predictable manner. Following the excitation of a slab current in the mixed layer, Gill (1984) used a normal-mode expansion to investigate the linear response of the ocean interior. By projecting a step velocity profile (to mimic a mixed layer that has been accelerated by the wind) onto the flat-bottom dynamical modes, the amplitude of each mode is readily obtained using Gill’s (1984) Eq. (3.8). The modes are computed by solving a Sturm–Liouville equation following standard methods (e.g., Alford and Zhao 2007) and the observed stratification (Fig. 5a). A few representative modes are plotted in Fig. 5b. It is apparent that our data, which only span the upper 800 m (gray), are not sufficient to separate the first few modes from each other or from a depth-independent flow.

The expected modal partition of the energy is sensitive to the mixed layer depth, as demonstrated by Gill (1984). For $\text{MLD} = 100 \text{ m}$, as typical at our location in wintertime, the most energy projects onto modes 2 and 3 (Fig. 7a, black), such that the first four modes should contain about 80% of the energy (Fig. 7b). For $\text{MLD} = 50 \text{ m}$, the fraction is reduced to about 50% (gray). Because we cannot measure the lateral energy flux in these lowest few modes, we will return to this point when

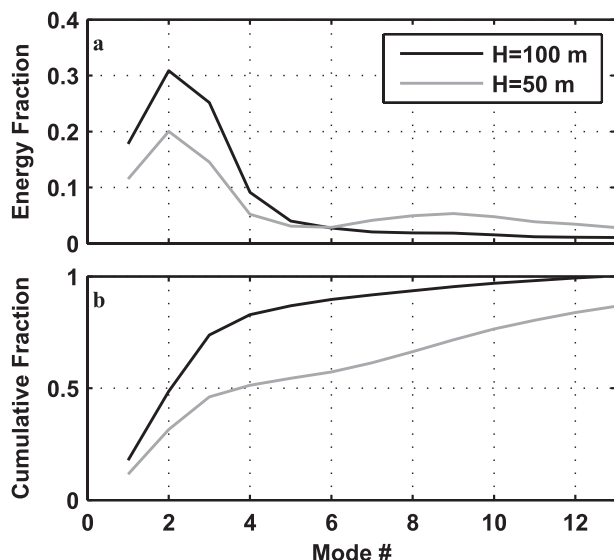


FIG. 7. The fraction of (a) energy and (b) its integral projecting onto each dynamical mode from Gill (1984) for MLDs of 100 and 50 m.

considering our estimates of the vertical flux to the deep sea.

3. Observed near-inertial signals

a. Overview

We next return to Fig. 2 in order to present the full record of total and near-inertial velocity. Total meridional velocity (Figs. 2c,d) shows a wide range of processes, including semidiurnal tides and mesoscale eddies with time scales of a few weeks. (Zonal velocity shows similar features and so is not shown.) At the lowest frequencies, meridional velocity is northward in the first year, gradually transitioning to southward in the second year. Semidiurnal signals are $10\text{--}20\text{ cm s}^{-1}$, too great to be barotropic tides (which are only about 2 cm s^{-1} according to predictions from the TPXO7.2 tidal model for this location). Their vertical wavelength is long, consistent with low-mode internal tides radiating northward from Hawaii, as observed at sites somewhat to the south (Alford and Zhao 2007).

The near-inertial response is evident even in the total velocity signals each fall and winter as a series of interference patterns sloping downward to the right. Because the interference patterns arise from interactions with the internal tide, they are seen more clearly in the bandpassed data (Figs. 2e,f). The near-inertial motions are strongly clockwise (CW) polarized, such that u_{in} and v_{in} are highly correlated with a lag of about 90° (not shown). To emphasize the envelope of the wave groups

rather than the individual crests, speed is plotted instead of v as above, so negative values are impossible.

The strongest near-inertial signals occur in winter of each year. These largely follow storms, which is loosely evident upon inspection of wind speed. However, given that the mixed layer response is given by the inertially resonant portion of the signals via (3), the time series of wind work (Fig. 4b, red) shows better correspondence with particular events than wind speed.

Following each storm, speed in the mixed layer rapidly increases to $0.5\text{--}0.6\text{ m s}^{-1}$ (saturating the color map), overwhelmingly dominated by near-inertial signals as evident by comparison of the raw and filtered amplitudes. Consistent with the intermittent input of energy from the wind (D'Asaro 1985 and Fig. 4), strong mixed layer signals are also intermittent, dominated by a few events.

Following the mixed layer events, radiation into the interior is evident as a set of discrete downward and rightward swaths (Figs. 2e,f, sloping black lines). It is clear that substantial energy penetrates deep in the record, but quantification of this statement (a major goal of our paper) requires a measure of the vertical energy flux F_z . Because we cannot compute F_z directly, we compute it as the product of the near-inertial energy and the vertical group velocity. The remainder of this section first characterizes the energy in terms of its frequency and wavenumber spectra and depth profiles and then examines the group velocity, which is computed for each of the observed downgoing wave events. Several of these are presented in detail before computing the group velocity for the whole set.

b. Frequency and wavenumber spectra

To propagate, the waves must be somewhat super-inertial. We therefore examine the frequency content of the signals via the frequency spectrum of WKB-scaled rotary velocity $u + iv$ (Mooers 1970; Gonella 1972). Spectra are computed at each depth using the sine multitaper method (Riedel and Sidorenko 1995), averaged together, and plotted in Fig. 8a. Prior to plotting, the spectrum is averaged over increasingly wide intervals with increasing frequency, as indicated by the narrowing of the confidence intervals (gray bars). The spectra are highly resolved, because of the long record. Positive and negative frequencies, corresponding to counterclockwise (CCW) and CW motions, are plotted in thin and thick lines, respectively.

The near-inertial waves evident in the unfiltered depth-time series (Figs. 2c,d) appear as a prominent peak at $-f$. Motion at this frequency is strongly polarized, with clockwise energy more than 200 times greater than counterclockwise. The width of the near-inertial peak results in

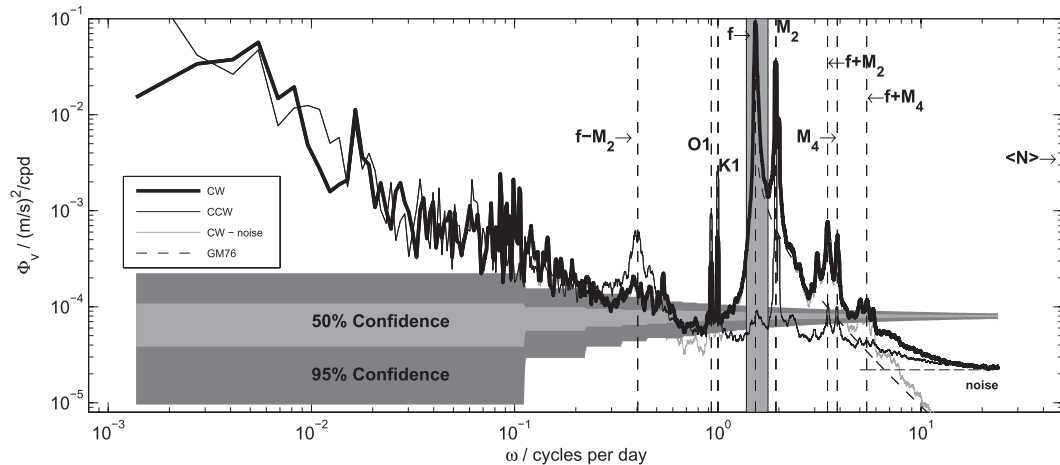


FIG. 8. Rotary frequency spectrum of WKB-scaled velocity. Multitaper spectral estimates using three tapers from 120- to 800-m depths are averaged together and then smoothed over even intervals in log frequency (see text); 95% and 50% confidence intervals are indicated. The near-inertial band used in bandpass filters and in later spectral closeup plots is shown in light gray. The GM76 model spectrum is indicated with a dashed curve. The noise floor of the ADCP measurements is indicated at high frequency with a horizontal dashed line. The light gray line is the measured CW spectrum with this noise floor subtracted.

part from the averaging over the many events, each of which has a slightly different frequency.

Substantial energy is also present at the semidiurnal (M_2 and S_2) and diurnal (K_1 and O_1) tidal frequencies. Each pair is easily separated given the long record, but it is difficult to see M_2 and S_2 separately in this display. All four peaks show similar polarization, with clockwise energy exceeding counterclockwise by about a factor of 5. As discussed above, the semidiurnal peaks are dominated by baroclinic internal tides. Because $|f|$ is greater than the diurnal frequencies at this latitude, the diurnal peaks must be barotropic tides or trapped baroclinic waves. Their amplitude and polarization are as expected from TPXO7.2, suggesting the former.

Strong peaks are also present at frequencies $-f \pm M_2$. As demonstrated by Alford (2001a), these can arise from kinematic interaction wherein the near-inertial motions are heaved up and down by tidal displacements. Alternately, they could arise from nonlinear interactions, where energy is transferred from the near-inertial and tidal peaks to the difference frequencies (Mihaly et al. 1998; van Haren et al. 1999, 2002; Guiles 2009). The peaks at $-f - M_2$ and $-f + M_2$ have levels within 15% of one another, implying the former, but a detailed analysis is beyond the scope of this paper. At the low latitude (6.5°S) considered by Alford (2001a), where $|f|$ is much less than the semidiurnal and diurnal tidal frequencies, the Doppler-shifted peaks were very close to the tidal frequencies. As will be shown, here the difference peak ($-f + M_2$) is at about 2.5 days, introducing a beating to the motions that will be visible in the

closeups to be presented below. Interestingly, its polarization is counterclockwise, though it arises entirely from internal wave processes with clockwise rotation. This is a consequence of the kinematic theory (Alford 2001a).

Between these peaks, the continuum spectrum is close to the Garrett and Munk (1975; as modified by Cairns and Williams 1976, hereafter referred to as GM76) level (dashed), before flattening near about $\omega_{\text{noise}} = 8$ cpd as the noise floor (1.5 and 2 cm s⁻¹ RMS for the upper and lower instruments, respectively; horizontal dashed line) of the instruments is reached.

The internal-wave motions ($0.95f < |\omega| < \omega_{\text{noise}}$) dominate the 2-yr spectra, containing 83% of the total energy in spite of the redness at low frequencies. The near-inertial motions, defined as frequencies $-(0.9-1.15)f$, contain 47% of the total. The band extends below $|f|$ in both of these cases to allow for potential raising and lowering of the “effective” inertial frequency, $f_{\text{eff}} = f + 1/2\zeta$, where ζ is the relative vorticity, by mesoscale motions (Weller 1982; Gill 1984; Kunze 1985).

The depth dependence of the peak shift is of key interest in what follows, because the vertical propagation of near-inertial waves depends sensitively on frequency,

$$c_{gz} = \frac{\omega^2 - f^2}{\omega m}, \quad (4)$$

where m is the vertical wavenumber. We thus examine the near-inertial portion of the spectrum more closely in Fig. 9a by plotting the region near $-f$ versus depth. Beginning at depths less than 100 m, which are in the

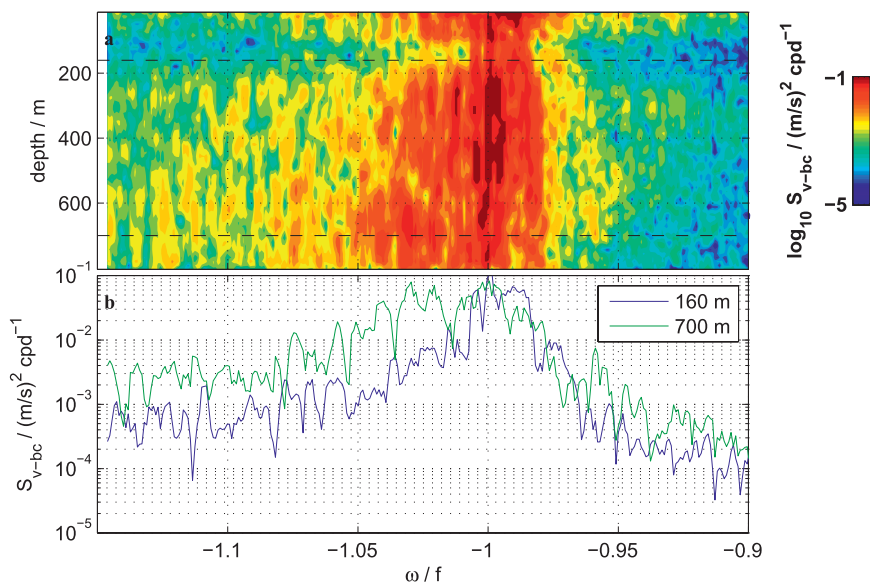


FIG. 9. (a) Rotary frequency spectrum of WKB-scaled velocity vs depth, zoomed in around the CW near-inertial frequency. The horizontal axis is normalized by f . Gray lines are the instrument depths in years 1 and 2. (b) Line plots of the spectrum at the two depths shown in (a). Dashed lines in (a) indicate depths of the spectra plotted in (b).

mixed layer for part of the record, a broad range of frequencies is seen. Near 160 m, below the maximum MLD, the peak sharpens before broadening and shifting to higher frequencies deeper in the water column (Fig. 9b, blue). By 700 m, the peak has broadened and shifted to about $-(1.02\text{--}1.03)f$ (Fig. 9b, green).

The peak shift places bounds on the lateral distance from which the motions can have propagated. If generated at the local inertial frequency, $\omega = -1.03f$ would indicate a generation site of 52.1°N , or 233 km away. We speculate that higher-frequency motions associated with higher latitudes may be less energetic because of Papa's location near the northern end of the storm track (Fig. 1).

The vertical wavenumber spectrum of velocity is examined next (Fig. 10a). Each profile of complex velocity is first WKB scaled and stretched from 120 to 800 m and then Fourier transformed. The resulting spectral estimates at all times are then averaged together. Following Leaman and Sanford (1975), positive and negative wavenumbers are associated with upward and downward energy propagation, which are plotted separately with black and gray curves, respectively. The spectrum for each is plotted for the full measured signals (thin) and the bandpassed near-inertial signals (thick lines).

Much of the discussion in the paper will focus on velocity (which is most closely related to energy), which is red in wavenumber, falling off approximately as $\approx m^{-2}$ as predicted by GM76 (dashed line). To see more detail, and for comparison with past results, the shear wavenumber

spectrum is also computed by multiplying by $(2\pi m)^2$ (Fig. 10b). The spectral level in wavenumber space is about twice that of GM76. The energy excess in wavenumber relative to GM76 but not in frequency spectra indicate that the wavenumber and frequency spectra are not separable (as pointed out by Pinkel 1984). Much of the energy at $\sim 100\text{--}300\text{-m}$ scales comes from the near-inertial peak, which is not well represented by GM76.

The wavenumber spectrum of near-inertially bandpassed, downgoing velocity and shear are redder than the full spectrum for each quantity, as also found by Leaman and Sanford (1975) and D'Asaro and Perkins (1984). In shear, the downward motions have a peak at $\approx 250\text{-m}$ scales in our observations. Downgoing near-inertial motions dominate the total at the larger scales, decreasing in importance until upward- and downward-propagating energy become equal at about 100-m scales.

The large bin size of the instrument introduces a $\text{sinc}^4(m)$ rolloff of its vertical wavenumber response beginning near scales of 100 m (Alford and Gregg 2001; Polzin et al. 2002). The plotted spectra are corrected for this response. The uncorrected spectrum is also plotted for the total upward-propagating motions (gray dashed). It differs little, showing that the correction is minor for the motions considered here, which have longer wavelengths.

c. Energy

Following bandpassing, it is straightforward to compute near-inertial kinetic energy (KE),

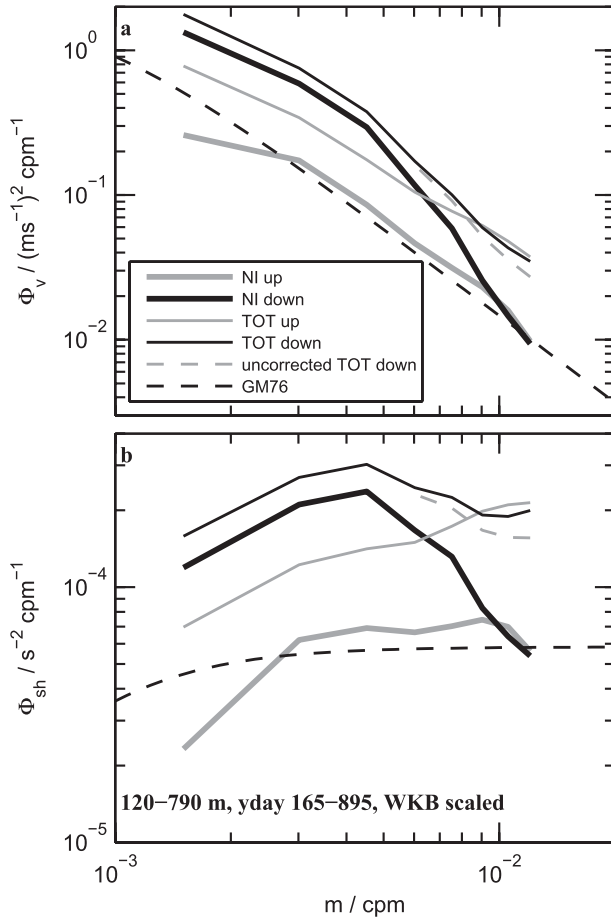


FIG. 10. Vertical wavenumber spectrum of (a) velocity and (b) shear for all frequencies (thin lines) and near-inertial frequencies (thick lines). Data have been WKB stretched and scaled. The GM76 spectrum is indicated in each panel with dashed lines. The effect of correcting the spectrum for the finite wavenumber response of the ADCP is shown (dashed line).

$$KE_{in} = \frac{1}{2} \rho_o |Z_{in}|^2, \tag{5}$$

and its WKB-scaled equivalent,

$$KE_{in}^{WKB} = \frac{\langle N \rangle}{N(z)} KE_{in}. \tag{6}$$

These are shown in the bottom two panels of Fig. 11. As clear from the velocity plot, energy is generally high in the mixed layer following each forcing event, followed by downward radiation. This is best seen in year 2 (Fig. 4), where directly measured wind work (Fig. 4c, red) is compared with near-inertial kinetic energy in the upper 300 m (Fig. 4e). Increases in mixed layer KE_{in} generally follow strong forcing events, as expected, but correspondence is not perfect between forcing amplitude

(wind work on mixed layer near-inertial motions) and the response. For example, mixed layer KE_{in} in early September and October 2009 increases sharply just after strong wind forcing events. However, the similarly strong March 2010 increase occurs in a time of more moderate forcing. The variability likely arises from differences in the lateral structure of the storms and mesoscale currents during the various events, which are of course not resolved by our single mooring. Energy is clearly higher in winter, but the timing and patterns in the two years are quite different. Overall, energy below the mixed layer is greater in year 2.

The depth dependence of the energy is examined next by averaging over summertime and wintertime periods (Fig. 12). Profiles are plotted as stacked histograms consisting of the semidiurnal, near inertial, and sum of all other frequencies. The near-inertial signals are further separated into upward- and downward-propagating motions via the positive and negative Fourier wavenumber components of complex velocity at each time. In wintertime, near-inertial signals are over half of the total KE at most depths. Downward-propagating signals exceed upward-propagating signals by a factor of 3–7, as first observed by Leaman and Sanford (1975). In summer, when wind forcing is weak, downward-propagating near-inertial energy still exceeds upward-propagating energy, but by a smaller factor (2–3). The total near-inertial energy is 5–6 times less (as also seen by Alford and Whitmont 2007), leading to a smaller fraction of the total (~25%).

All quantities decrease in depth, in large part because of WKB refraction. The WKB-scaled quantities (bottom), which remove this effect, generally show much less of this decay. The downgoing near-inertial signals, in particular, decay by a factor of ~1.5, which is again consistent with those observed at other sites by Alford and Whitmont (2007).

d. Case studies

Radiation occurs in a finite number of events, which are identified by hand and marked in Fig. 2d. The richness of the radiated fields is demonstrated by examining three of these in closeup (Figs. 13–15). In each, wind stress is first plotted (Figs. 13a, 14a, 15a). The near-inertial kinetic energy in the mixed layer (Figs. 13b, 14b, 15b, blue) is then compared to the time integral of the work done by the wind (green). For the first two cases, which are in year 2, wind work is computed from observed wind and inertial currents. For the third example, work from the NCEP-forced slab model is used.

Cumulative wind work is the strongest in the first example (Fig. 13), occurring in two distinct events on 21 and 25 October. The time integral of wind work (Fig. 13,

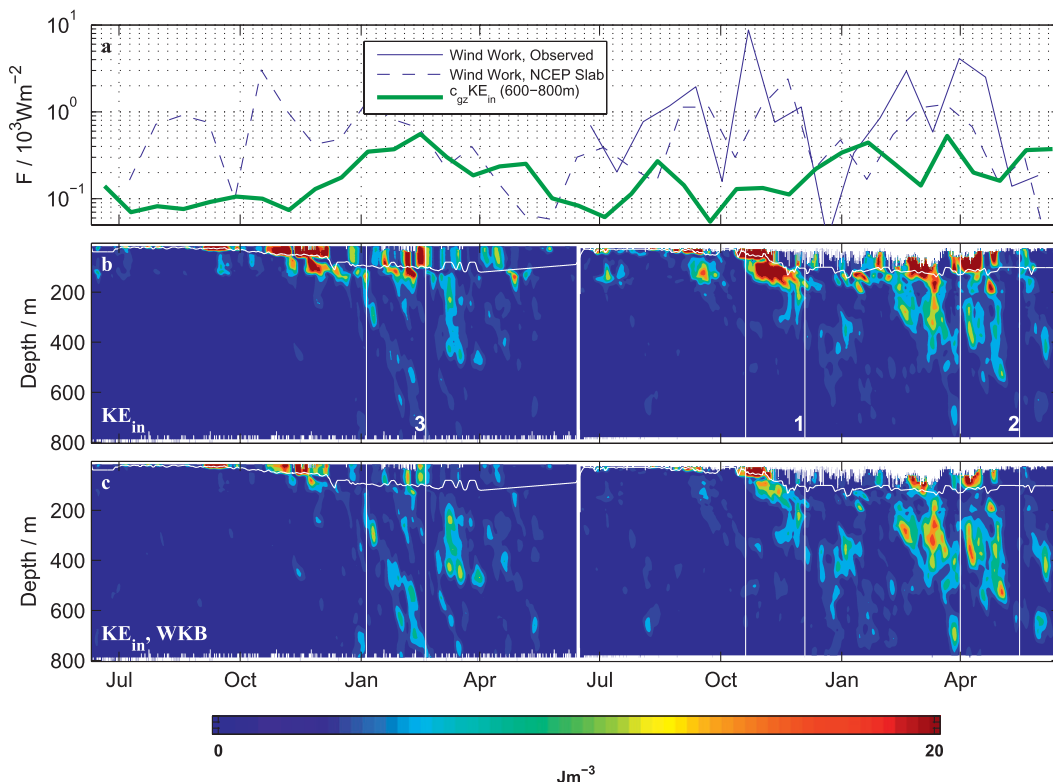


FIG. 11. (a) Observed wind work, MLD incorporated (blue line); NCEP slab wind work (dashed line); and the observed flux computed as the mean of energy from 600 to 800 m multiplied by $c_{gz} = 1.5 \times 10^{-4} \text{ m s}^{-1}$ (13 m day^{-1} ; green line). All have been smoothed over 20 days. (b) KE_{in} for the whole 2-yr record. (c) WKB version. The momentum-based MLD is overplotted in (b),(c) in white. Closeup periods plotted in Figs. 13–15 are shown.

blue) should equal the change in mixed layer KE (Fig. 13, red) minus dissipative and damping processes,

$$\int \Pi = \Delta \text{KE}_{\text{ML}} - (\text{damping} + \text{dissipation}). \quad (7)$$

Observed near-inertial KE (blue) is about 3 kJ m^{-2} at the start of the record, reflecting motions from previous forcing events. It rises during this period but less sharply, with a change of about $\frac{1}{2}$ – $\frac{3}{4}$ of the integrated wind work. Presumably, the rest is associated with damping (which includes radiation in this context). Following this, integrated work remains constant (indicating no more forcing), whereas mixed layer KE decays over the course of a week or so.

Observed and modeled mixed layer velocity (Fig. 13c) show good agreement in phase, as typically seen beginning with Pollard and Millard (1970). Observed amplitude is greater prior to 4 November partly because of the preexisting currents. Agreement is better later in the example.

Total and near-inertial meridional velocity (Figs. 13d,e) indicate a weak near-inertial packet radiating downward

to about 350 m over the next several weeks. However, energy deeper than 200 m (Fig. 13b, green) remains well below the integrated wind work and mixed layer KE.

In the second and third events, wind work is substantially less (note different scale in Fig. 13b; also recall that the work in the third event is an indirect estimate from NCEP). For the second event, mixed layer KE is again nonzero at the beginning of the time period, increasing at a similar rate as the integrated work. As in the first example, slab-model velocity (Fig. 13c) agrees very well in phase with observations. (Agreement is poorer for the third example, presumably because wind is from NCEP rather than measurements.) Modeled velocity decays faster in the second case than observed. Improved agreement would be obtained with smaller damping in the slab model, but, because the wind work is not significantly affected by choice of damping and the deep propagation is our focus, we have not attempted to tune the damping to match the mixed layer observations.

In both the second and third cases, much more prominent downward radiation is seen than in the first case. Particularly in the third event, it is clear that radiation penetrates at least to 800 m. The differences in its degree

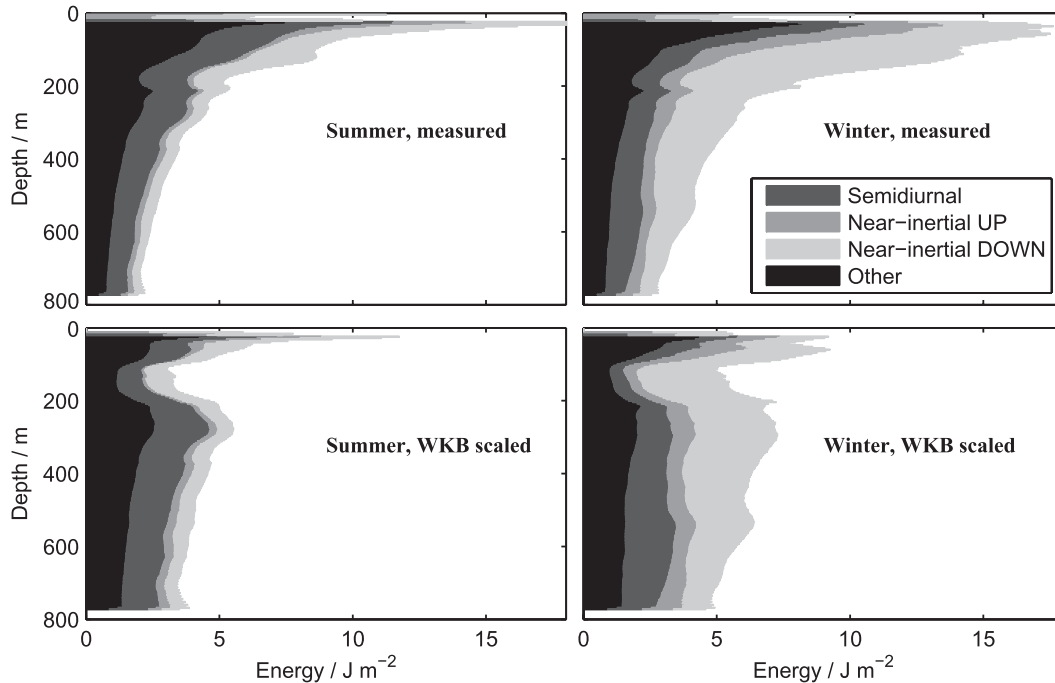


FIG. 12. Energy profiles for (left) summer and (right) winter, (top) measured and (bottom) WKB scaled.

between the three events and in general, upon examining the long time series, underscores the likely role of the lateral scales of the forcing and mesoscale flows, as made clear by the results of D'Asaro et al. (1995). Additionally, near-inertial currents present in the mixed layer prior to the storm, and waves propagating in from elsewhere can play a role (Plueddemann and Farrar 2006). The downward phase propagation observed at depth in Fig. 14 (implying upward energy propagation; also seen at depth by Alford 2010) are a reminder of the potential role of radiation from laterally remote sources and/or greater depths.

e. Group velocity for all events

Group velocity is next examined and compared to frequency and wavenumber for each of the wave packets identified in Figs. 2e,f. Packets are first identified by visual inspection in closeup plots similar to Figs. 13–15 as downward-sloping regions of elevated energy. For each, plane wave fits are used to estimate the frequency and wavenumber, following Alford and Gregg (2001). The downward migration of near-inertial energy is then used to estimate c_{gz} , as done by Leaman and Sanford (1975), Leaman (1976), D'Asaro and Perkins (1984), and Alford and Gregg (2001). Fits to packets appearing in the case studies are shown as downsloping lines with slope c_{gz} . Hatched lines indicate individual crests in the plane wave fits.

Note that the downward migration is apparent in both raw and filtered velocity. However, the 2.5-day tide near-inertial beat pattern discussed above, which is particularly evident in Fig. 15, creates apparent downward migration much steeper than reasonable. It is therefore vital to be cognizant of such interference patterns when doing these calculations.

The vertical group velocity of linear internal waves should obey the dispersion relation (4). To determine if our estimates are consistent with this prediction, we plot our vertical group velocity estimates versus frequency in Fig. 16 for weak events ($KE < 3 \text{ J m}^{-3}$; circles) and strong packets ($KE > 3 \text{ J m}^{-3}$; Fig. 16, \times symbol). Observed values do not show the expected frequency dependence predicted by (4) (Fig. 16, dashed line). This is not really surprising, given our errors in estimating frequency and wavenumber from the packets, which are of finite duration and vertical extent. However, the c_{gz} estimates are in the correct range for the observed frequencies observed. The mean over all events, $1.5 \times 10^{-4} \text{ m s}^{-1}$ (13 m day^{-1}), is therefore used below to estimate the vertical energy flux.

4. Wavenumber–frequency spectrum

The spatial and temporal scales of the signals are next examined via the wavenumber–frequency spectrum. Our primary motivation is partitioning energy into

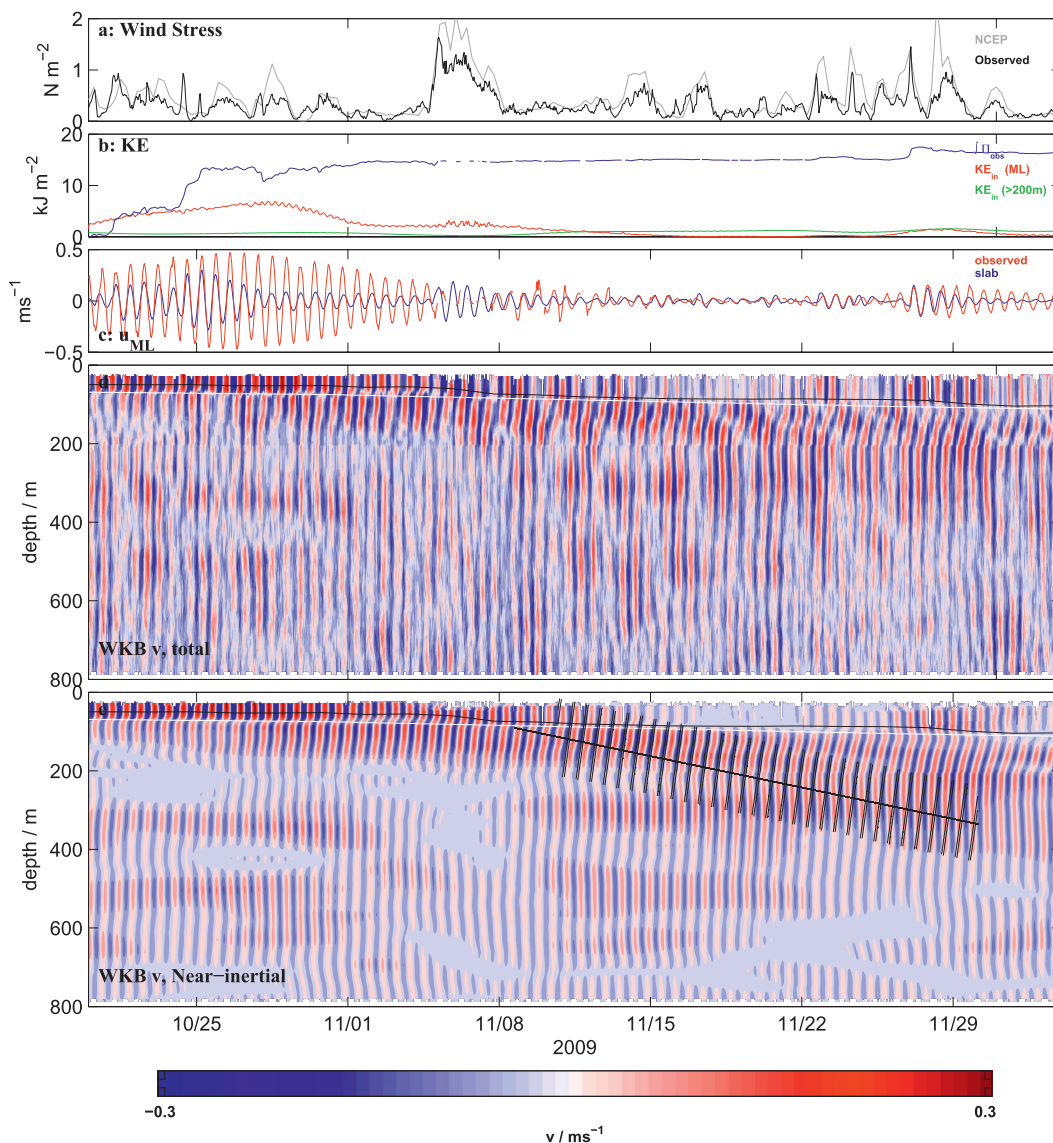


FIG. 13. (a) Wind stress from NCEP (gray) and the surface buoy (black). (b) Integrated observed wind work (blue), mixed layer near-inertial KE (red), and near-inertial KE deeper than 200 m (green) for event 1. (c) Zonal mixed layer current from observations (red) and predicted from the slab model (blue). (d) Total and (e) near-inertial meridional velocity. Sloping black lines are estimates of c_{gz} for each event by fitting the downward migration of energy in each. Phase lines from the plane wave fits are also plotted within ± 100 m of the packet center.

wavenumber and frequency bands for the group velocity and vertical energy flux calculation in the next section. However, the two-dimensional (2D) spectra are of interest in and of themselves and are thus discussed first. Spectral estimates are formed by computing the two-dimensional Fourier transform, $\tilde{w}(\omega, m)$, of the rotary velocity, $w(z, t) \equiv u + iv$, over the whole 2-yr record, as also done by Pinkel (1984) and van Haren (2006). To avoid the mixed layer, the depth range 120–800 m is used. Data are WKB scaled and stretched prior to transforming.

The wavenumber–frequency spectrum,

$$\Phi_{\text{vel}}(\omega, m) = \langle \tilde{w}\tilde{w}^* \rangle / (\Delta\omega\Delta m), \quad (8)$$

where $\Delta\omega$ and Δm are the frequency and vertical wavenumber resolution, respectively. Negative/positive frequencies and wavenumbers indicate clockwise/counterclockwise rotation in time and increasing depth, respectively. For freely propagating linear internal waves under well-stratified conditions, clockwise polarization with depth (negative frequency) indicates downward energy propagation.

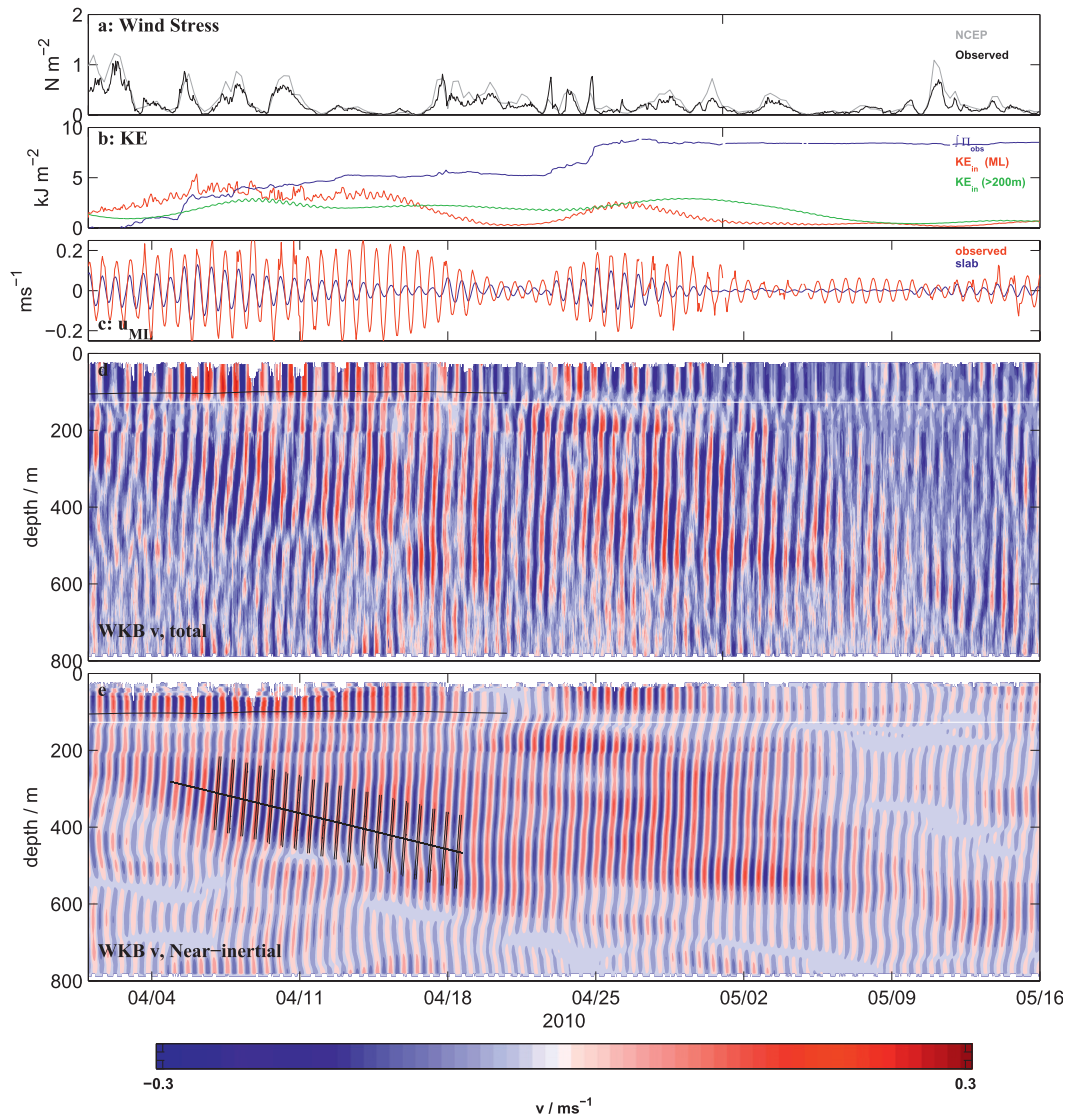


FIG. 14. As in Fig. 13, but for event 2. Note different plotting scales in (b),(c) from Fig. 13.

Though they were not computed in this manner, the rotary frequency and vertical wavenumber spectrum examined previously are given by integrals of this 2D spectrum,

$$\Phi_{\text{vel}}(\omega) = \int_{-m_N}^{m_N} \Phi_{\text{vel}}(\omega, m) dm \quad (9)$$

and

$$\Phi_{\text{vel}}(m) = \int_{-\omega_N}^{\omega_N} \Phi_{\text{vel}}(\omega, m) d\omega. \quad (10)$$

The 2D spectrum is plotted in Fig. 17a on a linear scale in wavenumber and frequency out to ± 0.3 cpm

and 2.5 cpd, respectively. It conveys a large amount of information (Pinkel 1984, 1985, 2008), some of which was discussed in the context of the separate wavenumber and frequency spectra: that is, (i) the dominance of energy at clockwise near-inertial and semidiurnal tidal frequencies, (ii) the weaker peak at $-f + M_2$ (2.5 days), and (iii) the redness in both ω and m . The subinertial barotropic tides, K_1 and O_1 , appear as narrow, long-wavelength peaks.

Though much can be learned from the 2D spectrum, we focus on the near-inertial motions of interest. To examine its detailed structure, the spectrum is plotted near the near-inertial peak (black rectangle) in Fig. 17b. To emphasize the departures from the inertial frequency, frequency is normalized by f . In this view, the dominance

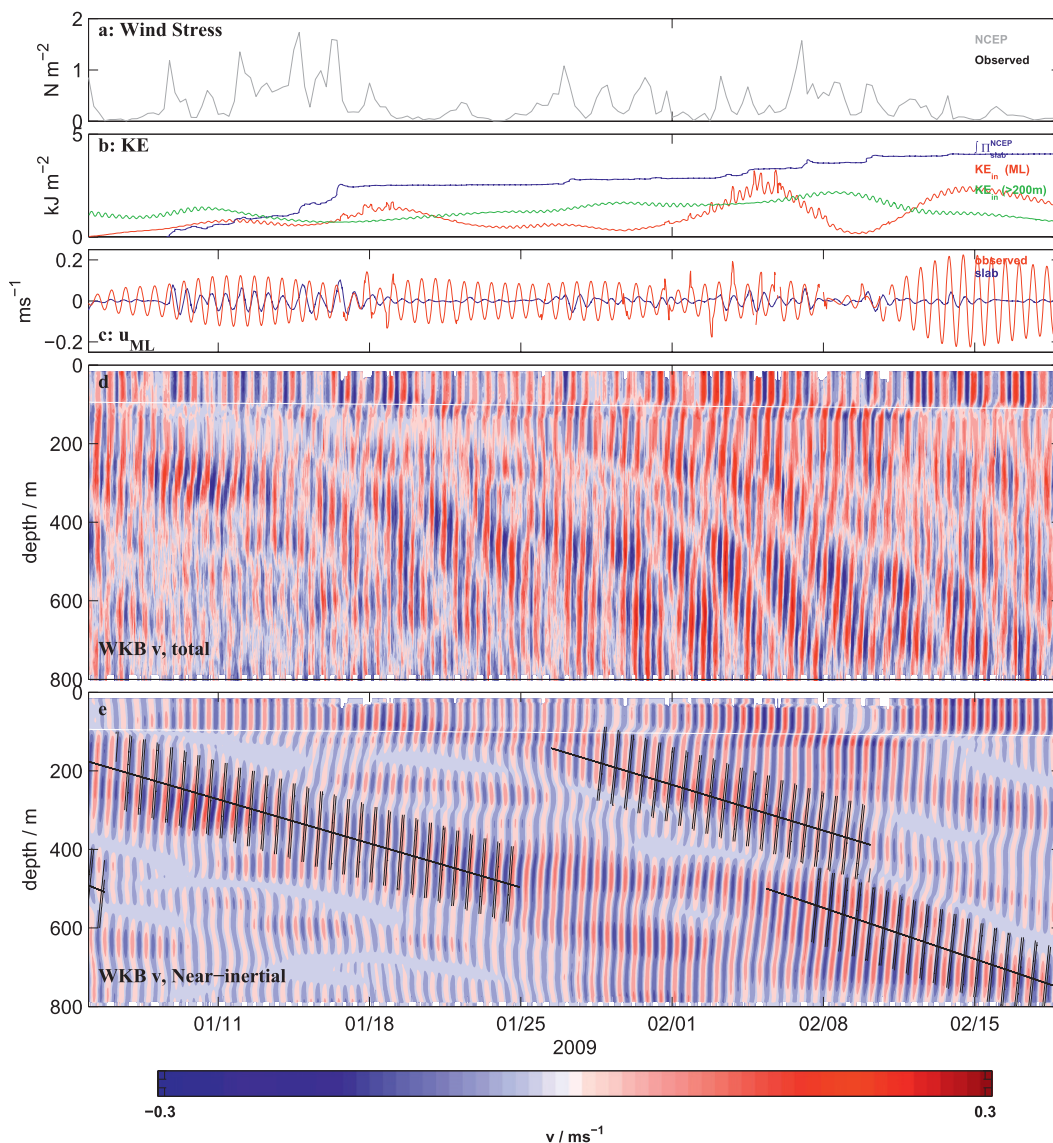


FIG. 15. As in Fig. 13, but for event 3. Note different plotting scales in (b),(c) from Figs. 13 and 14.

of the downward energy motions (negative m) is more visible. The motion is only very slightly superinertial at the peak wavenumber.

A good deal of energy, in fact, resides at subinertial frequencies. Energy at $|\omega| < f$ would not be expected to be freely propagating but rather could be the evanescent tail of waves near their turning latitude (Munk and Phillips 1968; Fu 1981). Alternately, the effective inertial frequency f_{eff} could have been lowered by a clockwise mesoscale or large-scale circulation, as discussed above. The circulation of the North Pacific subtropical gyre would have the correct sense of rotation but would probably be too weak to shift the peak sufficiently. For reference, a 2% shift in f would result from

a 20 cm s^{-1} current difference over 100 km. If brought on by mesoscale flows, an excess of transient clockwise-polarized eddies during the record would have the same effect on f_{eff} .

The other prominent feature in Fig. 17b is the downward slope toward lower absolute frequency, indicating connection between temporal and spatial scales of the respective downward- and upward-propagating motions. If f_{eff} were near $0.98f$, this would indicate that large-scale propagating motions are more superinertial, a signature of remote radiation. Specifically, only the long-wavelength motions can travel far from the generation site to latitudes where their frequency is greater than f at the generation site.

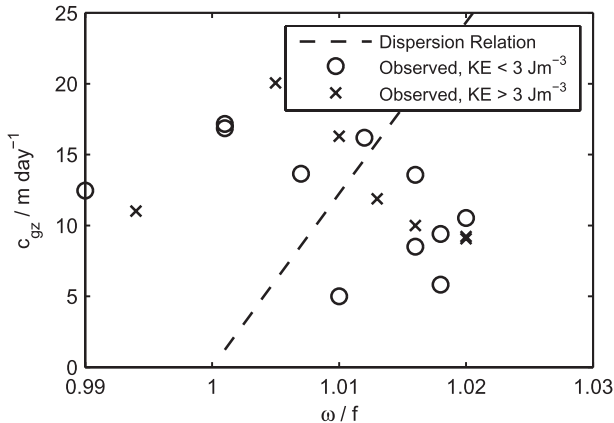


FIG. 16. Vertical group velocity estimated from the downward migration of energy for each group, plotted vs frequency estimated from the plane wave fits. The dashed line is the group velocity from the dispersion relationship for $\lambda = 400$ m.

5. Energy flux

Energy flux would best be estimated as the correlation between baroclinic pressure and vertical velocity $\langle wp \rangle$. Although neither w nor p is directly measurable in most situations, both can sometimes be estimated from observed density profiles from assuming they are hydrostatic (Althaus et al. 2003). In the most energetic internal waves, w can be measured directly from ADCP measurements. Here, vertical velocities are far too small to be detected by our instruments, and our density measurements at only two vertical locations preclude estimating either quantity. We therefore instead follow past work (Leaman and Sanford 1975; D’Asaro and Perkins 1984; Hebert and Moum 1994; Alford and Gregg 2001) and estimate vertical energy flux as $F_z = c_{gz}E$, where $E \approx \text{KE}$ is an excellent assumption for near-inertial waves.

Three methods are used to do the calculation, with results summarized in Table 1. The first method computes mean downgoing WKB-scaled KE from 200 to 600 m and from 600 to 800 m and simply multiplies these by the mean group velocity, $\bar{c}_{gz} = 1.5 \times 10^{-4} \text{ m s}^{-1}$ (13 m day^{-1}), estimated from the packet analysis. If all waves obey linear dynamics with no dissipation, energy should decrease as $N(z)$ in unstretched depth following WKB refraction, but c_{gz} should increase by the same amount such that the vertical energy flux remains constant in depth. In stretched depth, KE, c_{gz} , and F_z are constant. Because \bar{c}_{gz} is computed in stretched depth, we therefore use the WKB-scaled energy. Downward-propagating rather than total energy is used because upward-propagating waves presumably come from somewhere else and hence should not be compared with the local wind work. Estimates using the non-WKB-scaled quantities (not shown) are 10%–20% lower, whereas

those using the total rather than just the downgoing energy are 10%–15% higher.

The second method attempts to account for the variability in group velocity by summing WKB-stretched and WKB-scaled $\sum_i \text{KE}^i c_g^i$ over all observed events and dividing by the percentage of time occupied by the events. This method gives a similar answer to the first method. This agreement is encouraging, implying that 1) much of the energy flux is carried by the events identified in the packet analysis and 2) there is no correlation between group velocity and energy.

The third method uses the wavenumber–frequency spectrum to sum $c_{gz}E$ in wavenumber/frequency space. Because the group velocity is a function of vertical wavenumber and frequency, the total downward flux is computed by integrating

$$F_z = \int_0^{-m_N} \int_{\omega_L}^{\omega_U} c_{gz}(\omega, m) \Phi_{\text{vel}}(\omega, m) d\omega dm, \quad (11)$$

where the vertical group velocity is from the linear dispersion relation (4).

The integration is performed over the downgoing portions of the spectrum ($m < 0$) and over frequencies $-(1-1.15)f$. The frequencies contributing most to the flux are those $\approx -(1.05-1.1)f$, because of a competition between energy, which is strongly peaked at $|f|$, and group velocity, which increases away from $|f|$. To emphasize this, c_{gz} is contoured in Fig. 17b in black. Separate calculations are performed for years 1 and 2, with results of 0.23×10^{-3} and $0.50 \times 10^{-3} \text{ W m}^{-2}$, respectively.

The three methods generally give similar results (Table 1), spanning 0.16×10^{-3} – $0.23 \times 10^{-3} \text{ W m}^{-2}$ for year 1 and 0.19–0.50 for year 2. Taking these as rough bounds, the downward near-inertial energy flux in year 2 is between 12% and 33% of the directly computed wind work of $1.53 \times 10^{-3} \text{ W m}^{-2}$. Results for year 1 are similar but less meaningful because the wind work is not directly estimated.

Hence the annual averages indicate the flux transiting 800 m is a substantial portion of the wind work. How does this vary in time? Returning to Fig. 11, flux from the first method (green) is compared to the time series of wind work. In year 2, Π_{obs} is plotted (blue); $\Pi_{\text{slab}}^{\text{NCEP}}$ is plotted for both years (dashed). All have been smoothed with a 20-day running boxcar filter.

The percentage of wind work transmitted past 800 m is highly variable in time. In fall and winter, wind work during resonant forcing periods greatly exceeds the deep vertical energy flux. By March of each year, when deep vertical energy flux peaks, wind work is not as strong (partially because of the deeper mixed layers, which reduce the flux; D’Asaro 1985), such that the deep energy flux is a greater percentage of the forcing.

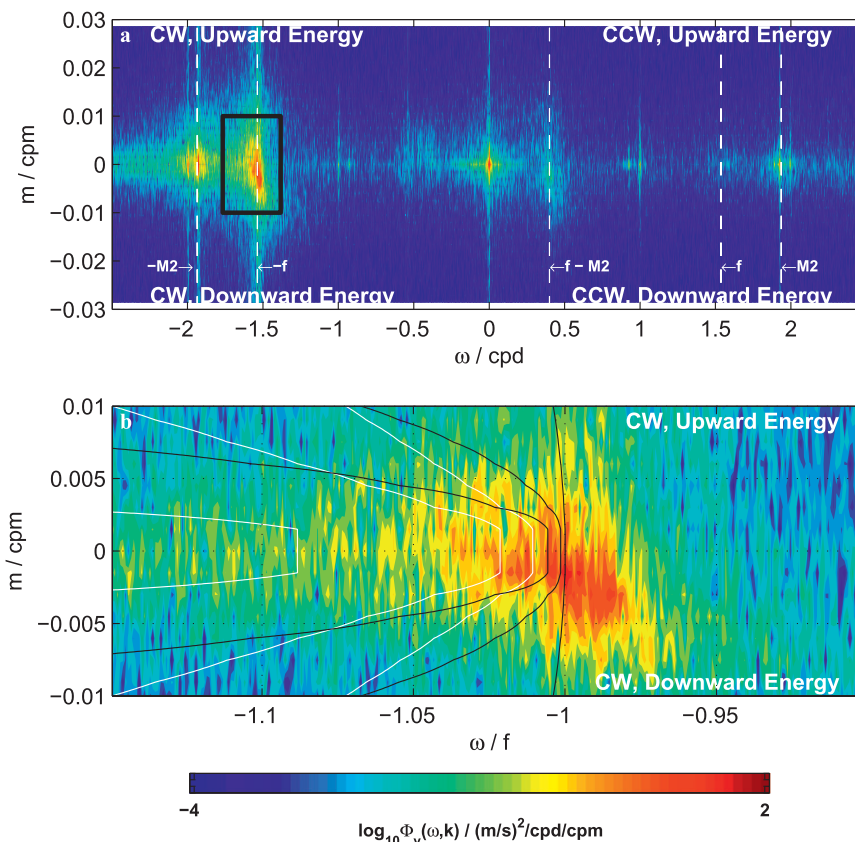


FIG. 17. Wavenumber–frequency spectrum of complex velocity, computed over the whole 2-yr record using depths 200–800 m. Inertial, semidiurnal, and diurnal tidal frequencies are indicated with vertical dashed lines. (b) Closeup of the near-inertial band. (a) Near-inertial band is indicated with vertical lines. Black and white lines in (b) are contours of vertical and horizontal group velocity, respectively. Contour levels are $(0.25, 0.5, 2) \times 10^{-3} \text{ m s}^{-1}$ for vertical group velocity and $(0.5, 2, 4) \times 10^{-2} \text{ m s}^{-1}$ for horizontal group velocity.

The variety of lateral scale and mesoscale conditions, which lead to the differences in the character of the near-inertial wake that is evident in the case studies examined, likely contribute to this variability. Unfortunately, the percentage cannot be computed for year 1 given our lack of direct wind measurements, but it seems likely that it would vary substantially from year to year.

6. Summary and discussion

We have presented 2 yr of observations of total and near-inertial velocity in the upper 800 m and demonstrated the variability in the character and structure of the downward-propagating motions. Both winters show marked downward radiation in late winter extending at least to the bottom of our record at 800 m. The degree of deep propagation varies substantially, which is sensible given the expected dependence of near-inertial propagation on lateral structures in both the storm forcing and

the mesoscale flows in the mixed layer. Unfortunately, we cannot address these dependences with data from a single mooring.

In an attempt to calculate the percentage of the energy put into near-inertial mixed layer motions by the

TABLE 1. Wind work and observed near-inertial flux estimates ($\times 10^{-3} \text{ W m}^{-2}$).

	Year 1	Year 2
Wind work estimates		
Observed currents: observed winds	—	1.53
Slab model: observed winds	—	1.30
Slab model: NCEP winds	1.30	0.93
Observed estimates of downward energy flux		
$\overline{c_{gz}^{-1}} \text{KE}_{\text{in}}^{\text{WKB}}$ (downward only: 200–600 m)	0.19	0.29
$\overline{c_{gz}^{-1}} \text{KE}_{\text{in}}^{\text{WKB}}$ (downward only: >600 m)	0.16	0.19
Summed over events: $\sum_i c_g^i \text{KE}^i$	0.23	0.21
Wavenumber–frequency spectrum	0.23	0.50

wind that transits 800 m and therefore potentially reaches the deep sea, we then used a variety of methods to estimate the downward flux of energy flux carried by the near-inertial motions. We compared these values to work done by the wind on inertial motions in the surface of the ocean, estimated with directly measured wind and near-inertial mixed layer velocity. The values and percentages vary greatly in time (Fig. 11), with annual-mean values ranging from 0.19×10^{-3} to $0.50 \times 10^{-3} \text{ W m}^{-2}$ for year 2 (12%–33% of the wind work; Table 1).

Taken simply, these numbers are estimates of the amount of near-inertial energy flux transiting 800 m toward the deep sea. If the higher value of $0.50 \times 10^{-3} \text{ W m}^{-2}$ dissipated evenly over the remaining 3400 m of the water column, it would result in a very modest dissipation value of

$$\bar{\epsilon} = \frac{F_{z,800\text{m}}}{(\rho)(3400 \text{ m})} = 1.5 \times 10^{-10} \text{ W kg}^{-1}$$

Alternately, if it dissipated in the bottom 500 m such as in a near-critical reflection or bottom boundary layer absorption, dissipation would be $10^{-9} \text{ W kg}^{-1}$, with an associated diffusivity $K_\rho = 0.2\bar{\epsilon}\bar{N}^{-2}$ (Osborn 1980) of about $5 \times 10^{-4} \text{ m}^2 \text{ s}^{-1}$. Because this is several times the value estimated long ago by Munk (1966) to maintain stratification in the abyssal ocean, our measurements suggest that near-inertial waves could play an important role in providing this energy. This is particularly so because Papa is not in a particularly strong region of wind forcing (Fig. 1).

On the other hand, these estimates underrepresent the potential for deep near-inertial mixing because they ignore 1) the substantial storm energy input directly at depth by projection onto the lower modes, which have no vertical energy flux, and 2) the lateral energy flux of these low-mode near-inertial motions. To illustrate these concepts, we consider a highly idealized time-mean budget for near-inertial energy,

$$-\mathbf{V} \cdot \mathbf{F}(x, y, z) = \epsilon(x, y, z), \quad (12)$$

where \mathbf{F} is the near-inertial energy flux and dissipation includes all processes removing energy from the near-inertial motions, including nonlinear interactions and turbulence. In this context, there is no source because the vertical component of \mathbf{F} includes the wind work at $z = 0$. Next, consider a slice of ocean extending a distance $L = 1000 \text{ km}$ in the meridional direction (synoptic scale). We envision the region to contain Papa and to extend north of the storm track (reasonable given Papa's location north of the strongest wind work; Fig. 1). Then, no flux enters the box through the northern boundary. If

we further assume that zonal fluxes are isotropic and that vertical flux and dissipation are independent of x and y , we can integrate in y to obtain

$$-\frac{\partial}{\partial z} F_z(z) - \frac{1}{L} F_y^{\text{south}}(z) = \epsilon(z). \quad (13)$$

That is, the vertical divergence of vertical energy flux is balanced at each depth by flux out the southern side of the box and dissipation.

Ignoring lateral fluxes for the moment, the difference between the wind work and the downward energy flux at 200 m would imply dissipation, likely at the base of the mixed layer, with a mean averaged over the upper 200 m of $6.2 \times 10^{-9} \text{ W kg}^{-1}$. Additionally, the observed decrease of approximately a factor of 2 in WKB-scaled vertical energy flux between 200 and 600 m (Table 1 and Fig. 12d, light gray) would imply a weak dissipation of about $2 \times 10^{-10} \text{ W kg}^{-1}$. These are both fairly small values compared to typical upper-ocean dissipation (e.g., Gregg 1989).

Alternately, the vertical flux divergence can be explained in terms of lateral energy flux divergence, estimated for our control volume as the flux out the south end of the box, which is not measured. However, an upper bound on the lateral flux carried by the vertical scales resolved in our data can be estimated using the same spectral method as was used for the vertical energy flux, assuming all energy is propagating toward the equator. The calculation is analogous to that for vertical group velocity using (11), but substituting the expression from the dispersion relationship for the horizontal group velocity,

$$c_{gx} = \frac{N}{m\omega}(\omega^2 - f^2)^{1/2}. \quad (14)$$

Contours of c_{gx} are plotted in white in Fig. 17b. For the downward- and upward-propagating near-inertial motions, we obtain a lateral energy flux from (11) and (14) between 120 and 800 m of 65 and 35 W m^{-1} , respectively, three orders of magnitude smaller than the vertical terms. This is not surprising because the longest wavelength resolved is only 680 m, approximately equivalent to mode 5 (Fig. 5). The higher modes do not carry much energy laterally (Nash et al. 2005).

The lower modes typically carry much greater lateral energy flux, with typical depth-integrated values of $O(1) \text{ kW m}^{-1}$ in the North Pacific (Alford 2003a). This is about $2/3$ of the 1.53 kW m^{-1} that would exit the south end of our control volume with the observed 1.53 m W m^{-2} of wind work, $L = 1000 \text{ km}$, and no dissipation. D'Asaro et al. (1995) were able to explain the observed loss of depth-integrated near-inertial energy in the Ocean Storms experiment in terms of lateral propagation of the first two modes, consistent with this scenario.

Therefore, dissipation and vertical and lateral propagation can together account for the energy input into near-inertial motions at the surface. The partition between them and the resulting depth and lateral distribution of near-inertial mixing must await more detailed measurements: necessarily with full depth coverage and some information on lateral structures.

Acknowledgments. This work was supported by the Office of Naval Research under Grant N00014-09-1-0401 and by the National Oceanic and Atmospheric Administration (NOAA). We are grateful to the captain, Murray McGregor, and the crew of R/V *Tully* and to the line P personnel for their assistance in coordinating the trips to station Papa. We thank Patrick A'Hearn, Robert Kamphaus, Michael Craig, Keith Ronnholm, and John Mickett for their assistance in preparing, deploying, and recovering the moored instrumentation and hardware. We thank the reviewers for valuable comments that greatly improved the submitted manuscript.

REFERENCES

- Alford, M. H., 2001a: Fine structure contamination: Observations and a model of a simple two-wave case. *J. Phys. Oceanogr.*, **31**, 2645–2649.
- , 2001b: Internal swell generation: The spatial distribution of energy flux from the wind to mixed layer near-inertial motions. *J. Phys. Oceanogr.*, **31**, 2359–2368.
- , 2003a: Energy available for ocean mixing redistributed through long-range propagation of internal waves. *Nature*, **423**, 159–163.
- , 2003b: Improved global maps and 54-year history of wind-work on ocean inertial motions. *Geophys. Res. Lett.*, **30**, 1424, doi:10.1029/2002GL016614.
- , 2010: Sustained, full-water-column observations of internal waves and mixing near Mendocino Escarpment. *J. Phys. Oceanogr.*, **40**, 2643–2660.
- , and M. Gregg, 2001: Near-inertial mixing: Modulation of shear, strain and microstructure at low latitude. *J. Geophys. Res.*, **106**, 16 947–16 968.
- , and M. Whitmont, 2007: Seasonal and spatial variability of near-inertial kinetic energy from historical moored velocity records. *J. Phys. Oceanogr.*, **37**, 2022–2037.
- , and Z. Zhao, 2007: Global patterns of low-mode internal-wave propagation. Part I: Energy and energy flux. *J. Phys. Oceanogr.*, **37**, 1829–1848.
- Althaus, A., E. Kunze, and T. Sanford, 2003: Internal tide radiation from Mendocino Escarpment. *J. Phys. Oceanogr.*, **33**, 1510–1527.
- Cairns, J. L., and G. O. Williams, 1976: Internal wave observations from a midwater float, 2. *J. Geophys. Res.*, **81**, 1943–1950.
- D'Asaro, E. A., 1985: The energy flux from the wind to near-inertial motions in the surface mixed layer. *J. Phys. Oceanogr.*, **15**, 1043–1059.
- , 1989: The decay of wind-forced mixed layer inertial oscillations due to the β effect. *J. Geophys. Res.*, **94**, 2045–2056.
- , 1995a: Upper-ocean inertial currents forced by a strong storm. Part II: Modeling. *J. Phys. Oceanogr.*, **25**, 2937–2952.
- , 1995b: Upper-ocean inertial currents forced by a strong storm. Part III: Interaction of inertial currents and mesoscale eddies. *J. Phys. Oceanogr.*, **25**, 2953–2958.
- , and H. Perkins, 1984: A near-inertial internal wave spectrum for the Sargasso Sea in late summer. *J. Phys. Oceanogr.*, **14**, 489–505.
- , C. E. Eriksen, M. D. Levine, P. Niiler, C. A. Paulson, and P. V. Meurs, 1995: Upper-ocean inertial currents forced by a strong storm. Part I: Data and comparisons with linear theory. *J. Phys. Oceanogr.*, **25**, 2909–2936.
- Egbert, G. D., and R. D. Ray, 2000: Significant dissipation of tidal energy in the deep ocean inferred from satellite altimeter data. *Nature*, **405**, 775–778.
- , and —, 2001: Estimates of M2 tidal energy dissipation from TOPEX/Poseidon altimeter data. *J. Geophys. Res.*, **106**, 22 475–22 502.
- , and S. Y. Erofeeva, 2002: Efficient inverse modeling of barotropic ocean tides. *J. Atmos. Oceanic Technol.*, **19**, 183–204.
- Fu, L.-L., 1981: Observations and models of inertial waves in the deep ocean. *Rev. Geophys. Space Phys.*, **19**, 141–170.
- Furuichi, N., T. Hibiya, and Y. Niwa, 2008: Model predicted distribution of wind-induced internal wave energy in the world's oceans. *J. Geophys. Res.*, **113**, C09034, doi:10.1029/2008JC004768.
- Garrett, C., 2001: What is the “near-inertial” band and why is it different from the rest of the internal wave spectrum? *J. Phys. Oceanogr.*, **31**, 962–971.
- , and W. Munk, 1975: Space-time scales of internal waves: A progress report. *J. Geophys. Res.*, **80**, 291–297.
- Gill, A. E., 1984: On the behavior of internal waves in the wake of a storm. *J. Phys. Oceanogr.*, **14**, 1129–1151.
- Gonella, J., 1972: A rotary-component method for analysing meteorological and oceanographic vector time series. *Deep-Sea Res.*, **19**, 833–846.
- Gregg, M. C., 1989: Scaling turbulent dissipation in the thermocline. *J. Geophys. Res.*, **94**, 9686–9698.
- , T. B. Sanford, and D. P. Winkel, 2003: Reduced mixing from the breaking of internal waves in equatorial waters. *Nature*, **422**, 513–515.
- Guiles, M. D., 2009: Energy redistribution through tidal and inertial wave interaction. Ph.D. thesis, University of Hawaii at Manoa, 241 pp.
- Hebert, H., and J. Moum, 1994: Decay of a near-inertial wave. *J. Phys. Oceanogr.*, **24**, 2334–2351.
- Jiang, J., Y. Lu, and W. Perrie, 2005: Estimating the energy flux from the wind to ocean inertial motions: The sensitivity to surface wind fields. *Geophys. Res. Lett.*, **32**, L15610, doi:10.1029/2005GL023289.
- Johnston, T. M. S., and D. L. Rudnick, 2009: Observations of the transition layer. *J. Phys. Oceanogr.*, **39**, 780–797.
- Kroll, J., 1975: The propagation of wind-generated inertial oscillations from the surface to the deep ocean. *J. Mar. Res.*, **33**, 15–51.
- Kunze, E., 1985: Near-inertial wave propagation in geostrophic shear. *J. Phys. Oceanogr.*, **15**, 544–565.
- Large, W. G., and S. Pond, 1981: Open ocean momentum flux measurements in moderate to strong winds. *J. Phys. Oceanogr.*, **11**, 324–336.
- Leaman, K. D., 1976: Observations on the vertical polarization and energy flux of near-inertial waves. *J. Phys. Oceanogr.*, **6**, 894–908.
- , and T. B. Sanford, 1975: Vertical energy propagation of inertial waves: A vector spectral analysis of velocity profiles. *J. Geophys. Res.*, **80**, 1975–1978.

- Levitus, S., and T. Boyer, 1994: *Temperature*. Vol. 4, *World Ocean Atlas 1994*, NOAA Atlas NESDIS 4, 117 pp.
- Mihaly, S. F., R. Thomson, and A. B. Rabinovich, 1998: Evidence for nonlinear interaction between internal waves of inertial and semidiurnal frequency. *Geophys. Res. Lett.*, **25**, 1205–1208.
- Moehlis, J., and S. G. Llewellyn-Smith, 2001: Radiation of mixed layer near-inertial oscillations into the ocean interior. *J. Phys. Oceanogr.*, **31**, 1550–1560.
- Mooers, C. N. K., 1970: The interaction of an internal tide with the frontal zone in a coastal upwelling region. Ph.D. thesis, Oregon State University, 505 pp.
- Munk, W., 1966: Abyssal recipes. *Deep-Sea Res.*, **13**, 707–730.
- , and N. Phillips, 1968: Coherence and band structure of inertial motion in the sea. *Rev. Geophys.*, **6**, 447–472.
- , and C. Wunsch, 1998: Abyssal recipes II: Energetics of tidal and wind mixing. *Deep-Sea Res. I*, **45**, 1977–2010.
- Nash, J. D., M. H. Alford, and E. Kunze, 2005: Estimating internal-wave energy fluxes in the ocean. *J. Atmos. Oceanic Technol.*, **22**, 1551–1570.
- Osborn, T. R., 1980: Estimates of the local rate of vertical diffusion from dissipation measurements. *J. Phys. Oceanogr.*, **10**, 83–89.
- Pinkel, R., 1984: Doppler sonar observations of internal waves: The wavenumber–frequency spectrum. *J. Phys. Oceanogr.*, **14**, 1249–1271.
- , 1985: A wavenumber–frequency spectrum of upper ocean shear. *J. Phys. Oceanogr.*, **15**, 1453–1469.
- , 2008: Advection, phase distortion, and the frequency spectrum of finescale fields in the sea. *J. Phys. Oceanogr.*, **38**, 291–313.
- Plueddemann, A. J., and J. T. Farrar, 2006: Observations and models of the energy flux from the wind to mixed layer inertial currents. *Deep-Sea Res.*, **53**, 5–30.
- Pollard, R. T., and R. C. Millard, 1970: Comparison between observed and simulated wind-generated inertial oscillations. *Deep-Sea Res.*, **17**, 153–175.
- Polzin, K., E. Kunze, J. Hummon, and E. Firing, 2002: The finescale response of lowered ADCP velocity profiles. *J. Atmos. Oceanic Technol.*, **19**, 205–224.
- Price, J. F., R. A. Weller, and R. Pinkel, 1986: Diurnal cycling: Observations and models of the upper ocean response to diurnal heating, cooling, and wind mixing. *J. Geophys. Res.*, **91**, 8411–8427.
- Riedel, K. S., and A. Sidorenko, 1995: Minimum bias multiple taper spectral estimation. *IEEE Trans. Signal Process.*, **43**, 188–195.
- Silverthorne, K. E., and J. M. Toole, 2009: Seasonal kinetic energy variability of near-inertial motions. *J. Phys. Oceanogr.*, **39**, 1035–1049.
- van Haren, H., 2006: Asymmetric vertical internal wave propagation. *Geophys. Res. Lett.*, **33**, L06618, doi:10.1029/2005GL025499.
- , 2007: Longitudinal and topographic variations in North Atlantic tidal and inertial energy around latitudes $30 \pm 10^\circ\text{N}$. *J. Geophys. Res.*, **112**, C10020, doi:10.1029/2007JC004193.
- , L. Maas, J. T. F. Zimmerman, H. Ridderinkhof, and H. Malschaert, 1999: Strong inertial currents and marginal internal wave stability in the central North Sea. *Geophys. Res. Lett.*, **26**, 19, 2993–2996.
- , L. Mass, and H. van Aken, 2002: On the nature of internal wave spectra near a continental slope. *Geophys. Res. Lett.*, **29**, 1615, doi:10.1029/2001GL014341.
- Watanabe, M., and T. Hibiya, 2002: Global estimates of the wind-induced energy flux to inertial motions in the surface mixed layer. *Geophys. Res. Lett.*, **29**, 1239, doi:10.1029/2001GL014422.
- Weller, R. A., 1982: The relation of near-inertial motions observed in the mixed layer during the JASIN (1978) experiment to the local wind stress and to the quasi-geostrophic flow field. *J. Phys. Oceanogr.*, **12**, 1122–1136.
- Wunsch, C., and R. Ferrari, 2004: Vertical mixing, energy and the general circulation of the oceans. *Annu. Rev. Fluid Mech.*, **36**, 281–314.
- Young, W., and M. Ben Jelloul, 1997: Propagation of near-inertial oscillations through a geostrophic flow. *J. Mar. Res.*, **55**, 735–766.
- Zervakis, V., and M. Levine, 1995: Near-inertial energy propagation from the mixed layer: Theoretical considerations. *J. Phys. Oceanogr.*, **25**, 2872–2889.